JACS
JOURNAL OF THE AMERICAN CHEMICAL SOCIETY

Article

pubs.acs.org/JACS

Predicting Morphologies of Solution Processed Polymer:Fullerene Blends

Sandra Kouijzer,[†] Jasper J. Michels,[‡] Mauricio van den Berg,[†] Veronique S. Gevaerts,[†] Mathieu Turbiez,[§] Martijn M. Wienk,[†] and René A. J. Janssen*[,†]

[†]Molecular Materials and Nanosystems, Eindhoven University of Technology, P.O. Box 513, 5600 MB Eindhoven, The Netherlands

[‡]Holst Centre/TNO, High Tech Campus 31, 5656 AE Eindhoven, The Netherlands

[§]Organic Electronic Materials Basel, BASF Schweiz AG, Schwarzwaldallee 215, 4002 Basel, Switzerland

Supporting Information

ABSTRACT: The performance of solution processed polymer:fullerene thin film photovoltaic cells is largely determined by the nanoscopic and mesoscopic morphology of these blends that is formed during the drying of the layer. Although blend morphologies have been studied in detail using a variety of microscopic, spectroscopic, and scattering techniques and a large degree of control has been obtained, the current understanding of the processes involved is limited. Hence, predicting the optimized processing conditions and the corresponding device performance remains a challenge. We present an experimental and modeling study on blends of a small band gap diketopyrrolopyrrole-quinquethiophene alternating copolymer (PDPP5T) and [6,6]-phenyl-C_{71}-butyric acid methyl ester ([70]PCBM) cast from chloroform solution. The model uses the homogeneous Flory–Huggins free energy of the multicomponent blend and accounts for interfacial interactions between (locally) separated phases, based on physical properties of the polymer, fullerene, and solvent. We show that the spinodal liquid–liquid demixing that occurs during drying is responsible for the observed morphologies. The model predicts an increasing feature size and decreasing fullerene concentration in the polymer matrix with increasing drying time in accordance with experimental observations and device performance. The results represent a first step toward a predictive model for morphology formation.

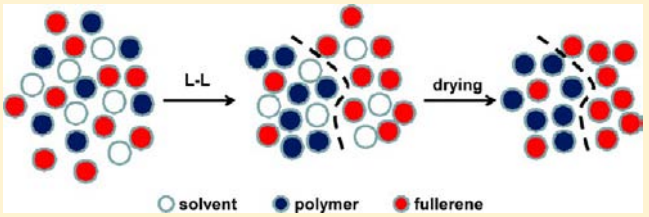

1. INTRODUCTION

The power conversion efficiency (PCE) of solution processed organic photovoltaics (OPV) has rapidly increased in previous years, and the highest reported efficiency for polymer:fullerene solar cells is now 9.2% for single and 10.6% tandem junction devices.[1,2] Combined with the promise of fast roll to roll processing on flexible substrates, OPV has potential as a future source of renewable energy.[3] A major contribution to the surge of power conversion efficiencies has come from developing new semiconducting polymers with a wider absorption range and higher quantum efficiencies for charge transfer and charge collection in photoinduced electron-transfer reactions with fullerene derivatives.[4−6] These new semiconducting polymers have finely tuned optical band gaps (E_g) and ionization potentials that serve to optimize the product of short-circuit current density (J_{sc}) and open-circuit voltage (V_{oc}) by absorbing a significant part of the solar spectrum and minimizing the energy loss ($E_g - V_{oc}$) in the photon to electron conversion.

Another crucial ingredient in making efficient solar cell is the morphology of the active layer. The intimacy of mixing, the size and composition of phase separated domains, their crystalline character, the concentration gradient in the vertical direction, and the presence of percolation pathways all have been considered important aspects in optimizing the photoactive layer of photovoltaic blends.[7−10] The blends are typically produced by solution-based processing such as spin coating, doctor blading, spray coating, inkjet printing, or slot dye coating. To reach the optimized blend morphologies, the choice of the solvent,[11] co-solvent,[12,13] processing additive,[14] drying time,[15,16] the solute concentration, and subsequent thermal[17] or solvent vapor annealing[18] all have been found important. Finding the right processing conditions is as much a challenge as designing the right molecular structure for phase separation.

Several techniques have been developed to study the bulk morphology. Atomic force microscopy (AFM), scanning Kelvin probe microscopy (SKPM), transmission electron microscopy (TEM), and electron tomography have been used to directly image the surface or the three-dimensional volume of the blends, while a variety of scattering techniques based on X-ray diffraction or neutron reflectivity have been used to gather structural information.[19] In addition, reports are addressing the time evolution of morphology formation during drying. Schmidt-Hansberg et al. have studied the drying process of solar polymer:fullerene solar cells.[16,20] For mixtures of poly(3-hexylthiophene) (P3HT) and [6,6]-phenyl-C_{61}-butyric acid

Received: June 1, 2013
Published: July 17, 2013

   dx.doi.org/10.1021/ja405493j | J. Am. Chem. Soc. 2013, 135, 12057−12067

methyl ester ([60]PCBM), it was shown that [60]PCBM crystallizes at the final stage of drying, although its solubility limit is reached in a very early stage.[16] For poly[(4,4-bis(2-ethylhexyl)dithieno[3,2-*b*:2′,3′-*d*]silole)-2,6-diyl-*alt*-(2,1,3-benzothiadiazole)-4,7-diyl] (PSBTBT) and [6,6]-phenyl C_{71}-butyric acid methyl ester ([70]PCBM) in situ grazing incidence X-ray diffraction (GIXD) and laser reflectometry were used to investigate the nanomorphology and revealed that the blend is quite insensitive to the drying process and that higher temperatures can be used to increase drying rates without altering device performance.[20]

Remarkably, until now the understanding of the processes is rather phenomenological, and no model has been developed that can describe or predict the morphology based on physical properties of the polymer, fullerene, solvent, and processing conditions. This makes morphology optimization somewhat of a skill rather than a truly rational approach. Moreover, if such a model would exist, morphology could be calculated from measurable properties of the starting materials. In this way, optimization of device processing will take less time and is probably easier to translate from one coating technique to another.

To guide our thinking, we show in Figure 1 schematically the different phase separation processes that may occur during drying of a solution containing the two components: a semiconducting polymer and a fullerene derivative. Before the solvent has fully evaporated either liquid–liquid (L–L) or liquid–solid (L–S) demixing may occur. Failing either of these processes, the blend will likely end up in an intimately mixed morphology that can undergo subsequent solid–solid phase separation, e.g., induced by thermal annealing. Blends of P3HT and [60]PCBM, when spin coated from a fast evaporating solvent and subsequently annealed, are likely an example of this route.[16,21] On the other hand, when drying is slow, L–S demixing may occur. A well-known example is the formation of P3HT fibers in solution by adding a nonsolvent for the polymer with [60]PCBM present and subsequent casting of these preaggregated solutions.[22]A similar example is found for blends of (PCPDTBT) with [70]PCBM that give intimate blends when spin coated from chlorobenzene without using a processing additive, such as 1,8-diiodooctane (DIO).[14,23−25] However, in the presence of DIO, PCPDTBT tends to aggregate in solution and gives a more phase separated blend after casting.[23,24]

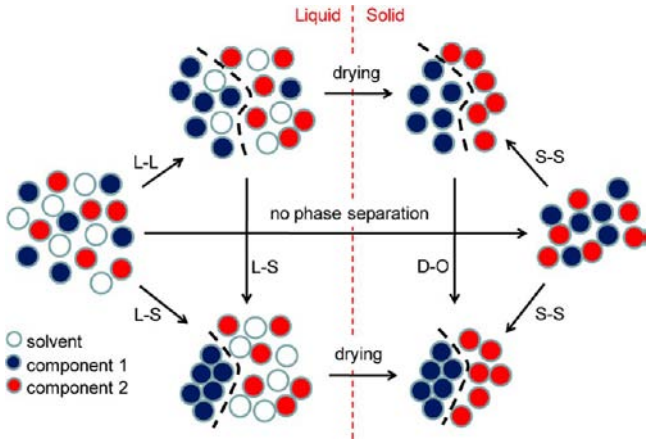

Figure 1. Schematic overview of the phase separation processes that may occurs during drying of a solution that contains two components. L–L, L–S, and S–S are liquid–liquid, liquid–solid, and solid–solid phase separations, respectively, and D–O is disorder–order transition.

Examples of L–L demixing during film formation are numerous. The first example is that of MDMO-PPV and [60]PCBM[11,26−28] or [70]PCBM.[29] When using solvents like toluene large (100–300 nm), almost circular domains of PCBM are formed in a matrix of polymer and fullerene. Similar results have been obtained for alternating polyfluorene (APFO) copolymers with [60]PCBM.[12,30,31] In fact, these large PCBM domains are encountered in many modern small band gap polymers based on, e.g., diketopyrrolopyrrole,[13,32] thienopyrroledione,[33] thienothiophene,[34] and iso-indigo[35−37] when processed from a single solvent. Typically these large PCBM domains afford suboptimal device performance. To reach higher performances with these novel small band gap polymers, typically co-solvents are used that result in more intimate blends. Examples are PTB7 which provides PCE = 9.2%,[1,34] PDTG-TPD with PCE = 8.5%,[33,38] and PDPP3T-*alt*-TPT with PCE = 8.0%.[39] Also for PBDTTPD which provides a high PCE = 8.5%, there is a positive effect of the processing agent, but less strong.[40] It is intriguing how a small amount of co-solvent can change the morphology and OPV performance so drastically, and there is discussion in the literature on the origin of the effect, but so far there is no adequate and consensual explanation for this rather general phenomenon. Before we can understand the role of the co-solvent, we first must understand in more detail how morphology formation occurs without the co-solvent. This is the topic of the present manuscript.

In this paper we investigate the phase separation formed in blends of a small band gap (E_g = 1.46 eV) diketopyrrolopyrrole-quinquethiophene alternating copolymer (PDPP5T)[41,42] with [70]PCBM (Figure 2) as an example of a modern small band gap polymer with relatively good PCE exceeding 5% when spin coated with [70]PCBM from chloroform containing 10 vol% *o*-dichlorobenzene (*o*-DCB) as co-solvent. However, when cast

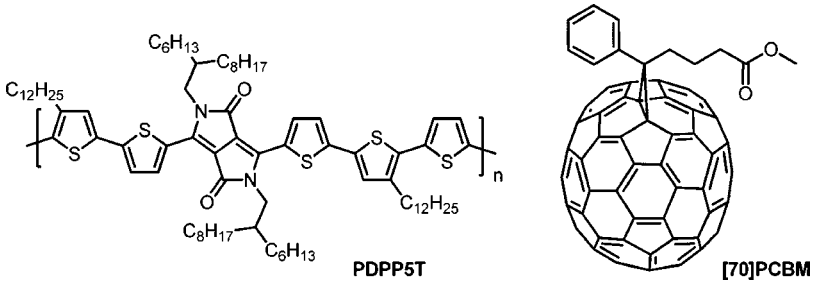

Figure 2. Molecular structures of PDDP5T and [70]PCBM.

dx.doi.org/10.1021/ja405493j | J. Am. Chem. Soc. 2013, 135, 12057−12067

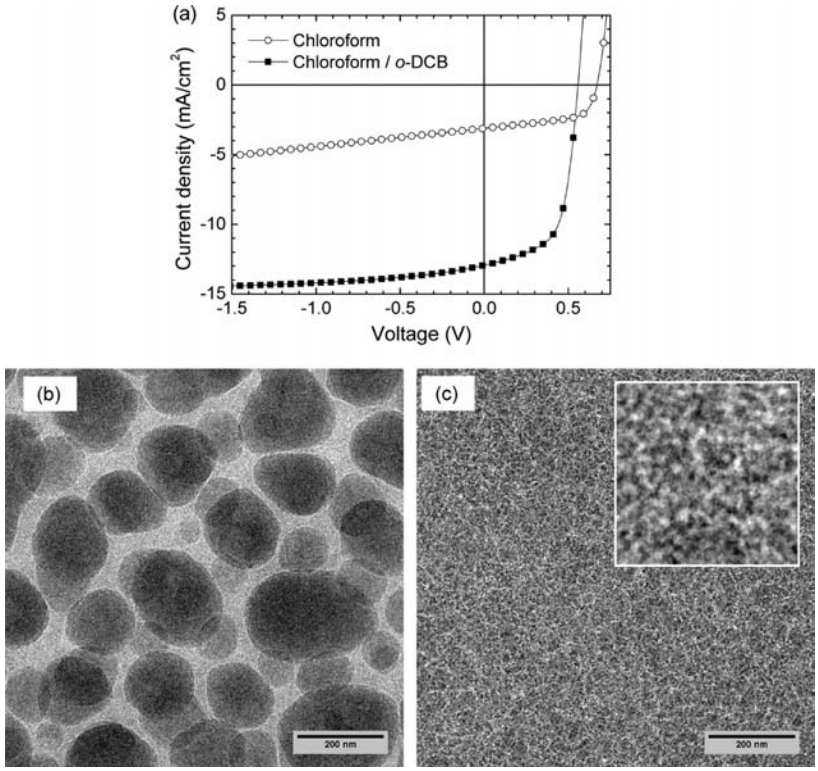

Figure 3. (a) *J*–*V* characteristics of PDPP5T:[70]PCBM blends cast from chloroform and from chloroform/*o*-DCB (9:1 v/v). (b) Bright-field TEM images of active layers from chloroform. (c) Same for chloroform/*o*-DCB (9:1 v/v). The scale bar in (b) and (c) corresponds to 200 nm. The inset in panel (c) shows the morphology at 4-fold higher magnification.

from pure chloroform solution these blends show L–L phase separation, and the PCE is much decreased. We find that the size of the domains varies with drying time. We investigate the PDPP5T:[70]PCBM morphology for different processing conditions with AFM and TEM and analyze the device performance. We then set up a theoretical model that uses the homogeneous Flory–Huggins free energy of the multicomponent blend, augmented with a square-gradient description to account for free energy contributions stemming from interfacial interactions between (locally) separated phases of the polymer, fullerene, and solvent to describe the phase separation process. We show that spinodal L–L demixing occurring during drying of the layer is responsible for the observed morphologies. The simulation results suggest an increasing feature size and decreasing fullerene concentration in the polymer matrix with increasing drying time in accordance with experimental observations and as such represents a first step toward a predictive morphology model.

2. RESULTS AND DISCUSSION

2.1. Active Layers Coated from Chloroform. Solar cells of photoactive PDPP5T:[70]PCBM layers, spin coated in a 1:2 weight ratio from chloroform and sandwiched between a transparent indium tin oxide (ITO) front electrode covered with poly(ethylenedioxythiophene):poly(styrene sulfonate) (PEDOT:PSS) and a reflective LiF/Al metal back electrode, provide a rather low optimized PCE of 1.3% (J_{sc} = 3.2 mA/cm^2, V_{oc} = 0.67 V, FF = 0.60). The performance is increased dramatically by addition of a co-solvent; with 10 vol % of *o*-DCB in chloroform, the PCE improves to 5.2% (J_{sc} = 13.8 mA/cm^2, V_{oc} = 0.57 V, FF = 0.67). The current density–voltage (*J*–*V*) curves for both cells shown in Figure 3a reveal that the main difference between the cells is a factor of 4 in current density.

The origin of these differences can be found in the morphology of the active layer. Figure 3b,c show bright-field TEM images of the active layers, where dispersed regions enriched in polycrystalline [70]PCBM show as darker and the polymer matrix as light gray. The blend layer spin coated from chloroform shows large, almost circular, agglomerates of [70]PCBM of 50–200 nm in diameter in a polymer matrix that may contain additional [70]PCBM. At some positions the [70]PCBM domains are clearly overlapping, suggesting that these domains do not extend over the entire thickness of the films. The size of the fullerene domains clearly exceeds the exciton diffusion length, and this morphology exhibits a too coarse phase separation to be able to generate a high current density. For the photoactive layer that is spin coated from the chloroform/*o*-DCB solvent mixture, the morphology is dramatically different. The [70]PCBM is finely intermixed with the polymer that shows a thin fibrillar network. Large pure [70]PCBM domains do not occur, and the current density and PCE (1.3% vs 5.2%) are much larger for devices made with these active layers. A similar fibrillar network has been observed for related DPP polymers and seems to be a characteristic morphology element for well-performing DPP-polymer:fullerene blends.[39,43]

Despite giving non-optimal cell performance, it is important to first understand on a more fundamental level the PDPP5T:[70]PCBM morphology formation from a single solvent (i.e., chloroform), before attempting to understand those made out of solvent mixture like chloroform/*o*-DCB. The lateral globular domains observed in polymer-PCBM blends processed, from a volatile solvent (i.e., chloroform), are likely due to a solvent

dx.doi.org/10.1021/ja405493j | J. Am. Chem. Soc. 2013, 135, 12057–12067

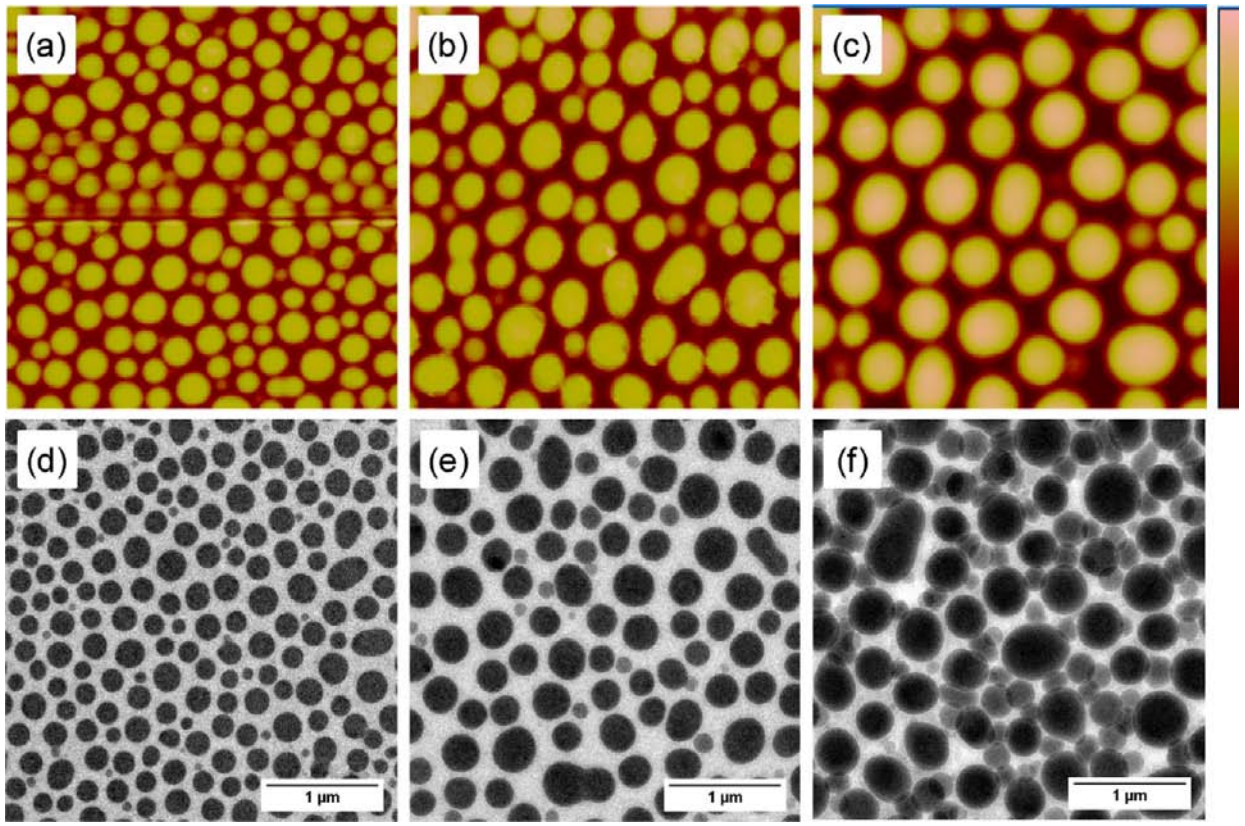

Figure 4. AFM (a, b, c) and TEM (d, e, f) images (3.5 × 3.5 μm) of 64 nm (a, d), 104 nm (b, e), and 180 nm (c, f) thick layers of PDPP5T:[70]PCBM spin coated from chloroform. Height scale is 80 nm in panel (a) and 100 nm in panels (b) and (c).

quench in the co-existence region of the phase diagram of the liquid ternary (i.e., solvent, polymer, and PCBM) mixture.[30] Due to the high solvent volatility and short drying time, competing mechanisms, such as L−S phase separation and crystallization, are suppressed. Hence, under those circumstances morphology evolution is controlled by L−L phase demixing, during which interfacial forces between different fluid phases determine domain size and shape. Moreover, although being random in general appearance, these morphologies usually seem to exhibit characteristic length scales, strongly indicative of a spinodal process governing the development of the microstructure.[30]

Varying the spin rate during coating of the $CHCl_3$:PDPP5T:[70]PCBM blend, while maintaining solids concentration, will affect the thickness of the active layer, where a higher spin rate results in thinner layers. More interestingly, Figure 4 also reveals that the domain size of the phase separation changes with spin rate. Both the AFM and TEM images show a strongly phase separated system with globular shapes. The thinnest layer shows many domains with sizes exceeding the exciton diffusion length multiple times. When the layer is thicker, the size of the domains further increases with an associated decrease in their number density. This observation strongly suggests that the blend components reside in a mobile state for a longer duration in case of a thick layer, allowing late stage domain coarsening via fluid-phase Ostwald ripening. The growth of domains with time was confirmed in an experiment where the layer was spin coated initially at a high rate (2000 rpm) first, followed by drying at a much slower rate (200 rpm). In this case the [70]PCBM domains were about 25% larger than when spin coating was at 2000 rpm, while the layer thickness remained similar as it is mainly determined by the initial spin rate. This gives further evidence that the blend morphology evolves from liquid-phase demixing. The height of the [70]PCBM-rich domains is twice as large as that of the matrix phase, independent of layer thickness. The TEM images show polycrystalline [70]PCBM dispersed in a matrix phase of (predominantly) PDPP5T. The TEM image of the thickest layer (Figure 4f) reveals some smaller agglomerates in between the larger ones. The smaller domains are not as thick as the larger ones, hence the lighter gray color. Some of these smaller domains also seem to overlap with each other or the larger domains.

To study the morphology in more detail, a thin ∼100 nm active layer was used to create a thin cross section sample made with a focused ion beam. The TEM image of the cross section (Figure 5, top) shows the active layer sandwiched between the PEDOT:PSS front electrode and the Li/F back electrode on Si wafer. Large [70]PCBM globules are embedded in the polymer-rich phase. A thin (>5 nm) skin layer of the matrix phase seems to be present between the [70]PCBM domains and the aluminum contact. On the PEDOT:PSS side, some blobs seem to touch the PEDOT:PSS, while others seem to be floating inside the matrix. For a thick ∼200 nm film, the [70]PCBM domains observed in the cross-section are larger laterally and vertically (Figure 5, bottom), consistent with the AFM results (Figure 4). Also for the thick films a skin layer can be seen that surrounds the domains at the top.

2.2. Simulating Liquid-Phase Demixing. Structure evolution in the OPV blend due to liquid-phase demixing can be modeled by extending the homogeneous (mean field) free energy expression of a multicomponent blend with terms

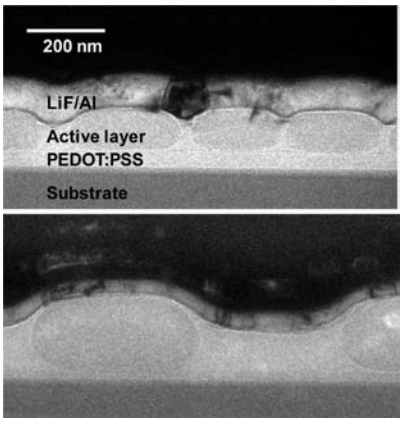

Figure 5. Cross section TEM image of a Si wafer with a layer stack of PEDOT:PSS|PDPP5T:[70]PCBM|LiF|Al and covered with Pt for thin (~100 nm, top) and thick (~200 nm, bottom) blend films. The size of the images is identical and shows that in the thicker films, the [70]PCBM domains are larger laterally and vertically. In both images the [70]PCBM domains seem to have a thin skin layer of PDPP5T-rich phase at the top and the bottom.

describing the interfacial interactions between (locally) separated phases, as proposed by Cahn and Hilliard.[44,45] For a ternary blend comprising two (polymeric) solutes and a solvent, the following phenomenological expression for the isothermal free energy density form has been proposed:[46,47]

$$F = \int \left(f_h(\varphi_i) + \frac{1}{2} \sum_{i=1}^{3} \kappa_i |\nabla \varphi_i|^2 \right) dV \tag{1}$$

Here, φ_i is the volume fraction of component i, $\nabla\varphi_i$ is the volume fraction gradient, and f_h is the homogeneous free energy, for instance given by the Flory–Huggins equation. According to Flory–Huggins theory,[48] the homogeneous (local) free energy density of a ternary blend reads on a per lattice segment (monomeric unit) basis:

$$\begin{aligned} f_h &= f_{FH} \\ &= \frac{kT}{v_{seg}} \left[\varphi_1 \ln(\varphi_1) + \frac{\varphi_2}{N_2} \ln(\varphi_2) + \frac{\varphi_3}{N_3} \ln(\varphi_3) + \chi_{12}\varphi_1\varphi_2 \right. \\ &\quad \left. + \chi_{13}\varphi_1\varphi_3 + \chi_{23}\varphi_2\varphi_3 \right] \end{aligned} \tag{2}$$

Here, kT is the thermal energy, v_{seg} is the volume of one lattice segment (in this work: $v_{seg} = v_{solvent}$), N_i is the number of lattice segments constituting one molecule of component i, and χ_{ij} is the dimensionless Flory–Huggins parameter representing the (enthalpic) interaction between components i and j. For this work we define: subscript 1 = $CHCl_3$, subscript 2 = PDPP5T, and subscript 3 = [70]PCBM. Flory–Huggins theory assumes the blend to be incompressible ($\varphi_1 + \varphi_2 + \varphi_3 = 1$), resulting in two mathematically independent volume fractions.

The second term in the integrand of eq 1 represents the non-local contributions to the free energy which result from the formation of concentration gradients upon phase separation. The strength of these contributions is expressed by the gradient energy coefficients κ_i. Substitution of eq 1 into the continuity equation, taking into account the incompressibility constraint and combined with a noise term yields the Cahn–Hilliard–Cook equations for the two independent volume fractions:[49,50]

$$\frac{\partial \varphi_2}{\partial t} = \nabla \cdot M_2 \nabla \left[\frac{\delta F}{\delta \varphi_2} \right] + \zeta_2 \tag{3}$$

$$\frac{\partial \varphi_3}{\partial t} = \nabla \cdot M_3 \nabla \left[\frac{\delta F}{\delta \varphi_3} \right] + \zeta_3 \tag{4}$$

Here, M_i is the mobility coefficient, related to the self-diffusivities D_i of the blend components according to $M_i = D_i(\partial^2 f^0_{FH}/\partial\varphi_i^2)^{-1}$,[51] where f^0_{FH} is the athermal homogeneous free energy ($\chi_{ij} = 0$). The exchange chemical potential $\delta F/\delta\varphi_i$ is given by the Euler–Lagrange equation:

$$\frac{\delta F}{\delta \varphi_i} = \frac{\partial f}{\partial \varphi_i} - \nabla \frac{\partial f}{\partial \nabla \varphi_i} \tag{5}$$

f being the integrand of eq 1. The terms ζ_i in eqs 3 and 4 represent spatially and temporally uncorrelated Langevin-type density fluctuations induced by thermal noise.[49]

In our simulations (for more details see Supporting Information) we use a two-dimensional (2D, top view) description and assume that all material transport exclusively takes place via diffusion, although flow-related phenomena cannot be excluded. Furthermore, the effective 2D top-view simulation geometry excludes any 3D and possible substrate- or air-interface-induced effects on demixing. We do acknowledge that in reality it is likely that stratified phase separation does take place at early times, as has been shown both experimentally and theoretically,[52−57] also for solvent-borne polymer/PCBM-based blends,[58−60] but for the present study, our aim is to focus on the mixing thermodynamics of the blend layer and the time-dependent composition of coexisting phases.

2.3. Flory–Huggins Interaction Parameters. The Flory–Huggins interaction parameters χ_{ij} used in the calculations were determined according to the approach used earlier by Moons et al.[30] This method is based on the determination of the surface energies of (spin coated) layers of pure polymer and PCBM using water contact angle measurements. The conversion of the measured contact angles into substrate surface energies was accomplished with Neumann's method.[61] For apolar materials a linear relationship exists between the (Hildebrand) solubility parameter (δ) and the square root of the surface energy (γ):

$$\delta = K\sqrt{\gamma} \tag{6}$$

where K is a more or less universal proportionality constant. Once the value of K has been established using known data on δ and γ of compounds of similar polarity, the Flory–Huggins interaction parameter may be evaluated according to the expression:

$$\chi_{ij} = \frac{v_{seg}}{kT}(\delta_i - \delta_j)^2 + \chi_s \tag{7}$$

Here, χ_s is the entropic contribution to the interaction parameter, which, for a nonpolar polymer in a nonpolar solvent, typically adopts a value between 0.3 and 0.4.[62] An often used value is $\chi_s = 0.34$. Its exact value did not significantly affect the outcome of the calculations performed in this work.

The measured surface energies of layers of pure PDPP5T and [70]PCBM are listed in Table 1, together with the proportionality constant $K = 116 \times 10^3$ $m^{-1/2}$, determined from independently measured literature data on δ and γ of compounds of similar polarity and chemical integrity, i.e.,

dx.doi.org/10.1021/ja405493j | J. Am. Chem. Soc. 2013, 135, 12057−12067

Table 1. Surface Energies, Solubility Parameters, and Proportionality Constants (see eq 7) Determined for Various Donor and Acceptor Materials

	γ (mN/m)	δ (MPa$^{1/2}$)	K ($\times 10^3$ m$^{-1/2}$)
PDPP5T	20.2[a]	16.5[a]	–
P3HT	26.9[b]	19.1[c]	116
PF8	25.3[d]	18.8[e]	118
[70]PCBM	35.8[a]	21.9[a]	–
[60]PCBM	35.4[f]	21.7[g]	115

[a]This work. [b]Ref 63. [c]Average of the values reported in ref 64. [d]Ref 30. [e]Ref 65. [f]Average of values reported in refs 30, 66, and 67. [g]Average of values reported in ref 64.

P3HT, poly(9,9-dioctylfluorenyl-2,7-diyl) (PF8), and [60]PCBM.

The resultant solubility parameters were then substituted in eq 7 to yield: $\chi_{23} = 1$ and $\chi_{12} = 0.4$ (Table 2), the latter using:

Table 2. Flory–Huggins Interaction Parameters and Effective Degrees of Polymerization for the $CHCl_3$/PDPP5T/[70]PCBM Ternary Blend[a]

χ_{12}	χ_{13}	χ_{23}	N_2	N_3
0.4	0.9	1	89	7

[a]Subscripts: 1 = $CHCl_3$, 2 = PDPP5T, and 3 = [70]PCBM.

$\delta_{CHCl_3} = 18.7$ MPa$^{1/2}$.[68] $\chi_{13} = 0.9$ was taken from literature[30] and is close to the value $\chi_{13} = 0.7$ obtained from our measurements. We verified that the actual value of χ_{13} does not affect the outcome of the modeling in a significant way. It is of interest to note that χ_{23} is comparable to the interaction parameter determined for the blend PF8:[60]PCBM ($\chi = 0.9$), which was shown to exhibit very similar lateral globular phase morphologies upon spin coating from a sufficiently volatile solvent.[30]

2.4. The Ternary Phase Diagram. To make predictions on the phase behavior of the ternary blend of $CHCl_3$:PDPP5T:[70]PCBM and to estimate the composition of coexisting phases, we calculated the liquid-phase ternary phase diagram using Flory–Huggins theory (eq 2). As input for this model, values of the three interaction parameters χ_{12}, χ_{13}, and χ_{23} (Table 2) as well as the effective degrees of polymerizations N_i of the blend components are required. The effective degrees of polymerization N_i were estimated considering the segmental site molar volume to be equal to the molar volume of one solvent molecule: $V_{m,CHCl_3}$ ~80 cm^3/mol (hence: $N_1 = 1$). Based on molecular modeling using ACD laboratories ChemSketch,[69] it was estimated that the solvent molecular volume is approximately equal to the volume of one thiophene ring (backbone), one DPP unit (backbone), and four CH_2 segments (side chains) of the PDPPP5T. The effective degree of polymerization N_2 was then obtained from the physical one, calculated from the average molecular weight determined by GPC and the molar mass of one DPP5T monomer.[70] N_3 was calculated by dividing the molar volume of [70]PCBM (calculated to be $V_{m,[70]PCBM}$ ~600 cm^3/mol) by $V_{m,CHCl_3}$. All input parameters for the Flory–Huggins model are listed in Table 2.

The ternary phase diagram (Figure 6) shows the division of composition space in single phase and coexistence regions separated by the binodal (blue line), obtained by the common

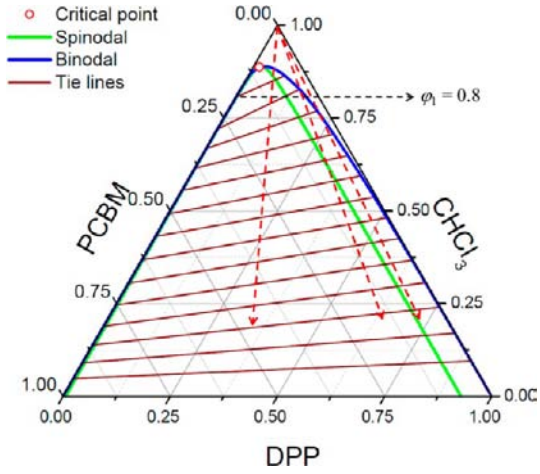

Figure 6. Ternary phase diagram of the $CHCl_3$:PDPP5T:[70]PCBM blend, calculated using Flory–Huggins theory; volume fractions of the three components are indicated on the axes; the blue and green lines represent the binodal and spinodal compositions, respectively; tie lines connect the compositions of corresponding phases at equal chemical potential; the dashed black line indicates the solvent quench depth assumed in the numerical simulations; the dashed red arrows indicate the change in blend composition upon solvent evaporation for a 1:2 (w/w), a 1:0.33, and a 1:0.12 (w/w) PDPP5T:[70]PCBM ratio, from left to right.

tangent construction. The limit of instability is indicated by the spinodal (green line), obtained analytically by solving $|(\partial^2 f_h)/(\partial\varphi^2)| = 0$. Using $|(\partial^3 f_h)/(\partial\varphi^3)| = 0$ the composition at the critical point was calculated to be: $\varphi_1 = 0.883$, $\varphi_2 = 0.032$, $\varphi_3 = 0.085$. Tie lines, given for various solvent volume fractions, connect the corresponding binodal compositions with equal chemical potential. The slope of the tie lines expresses the preference of the solvent for residing in the polymer-rich phase, rather than in the [70]PCBM-rich phase (originating from the significant difference between χ_{12} and χ_{13}, as $\chi_{12} < \chi_{13}$). Due to the fact that PDPP5T and [70]PCBM are only moderately compatible, as expressed by the relatively high value for χ_{23}, the single phase region covers only a small fraction of the phase diagram. In contrast, instability is expected for a considerable part of composition space. The left most arrow shows the trajectory followed upon solvent quenching and subsequent continued evaporation for a 1:2 (w/w) PDPP5T:[70]PCBM blend ratio. It indicates that this blend is likely to be quenched in the instable part of the coexistence region and would therefore decompose spinodically, as already hinted by the apparent presence of a characteristic length scale in the microscopic images of Figure 4.

Another striking feature is the pronounced asymmetry of the binodal, induced by the considerable size difference between PDPP5T and [70]PCBM. The important consequence is the presence of a significant fraction of [70]PCBM in the region of the polymer-dominated branch of the binodal located not too far from the critical point. In contrast, the corresponding [70]PCBM-dominated phase in this region is already quite pure. This observation indicates that, depending on the stage at which the phase separated morphology is kinetically frozen due to drying, more or less residual [70]PCBM may be present in the polymer-rich phase. We anticipate at this point that this can have a significant influence on the electronic characteristics of the OPV cell.

dx.doi.org/10.1021/ja405493j | J. Am. Chem. Soc. 2013, 135, 12057–12067

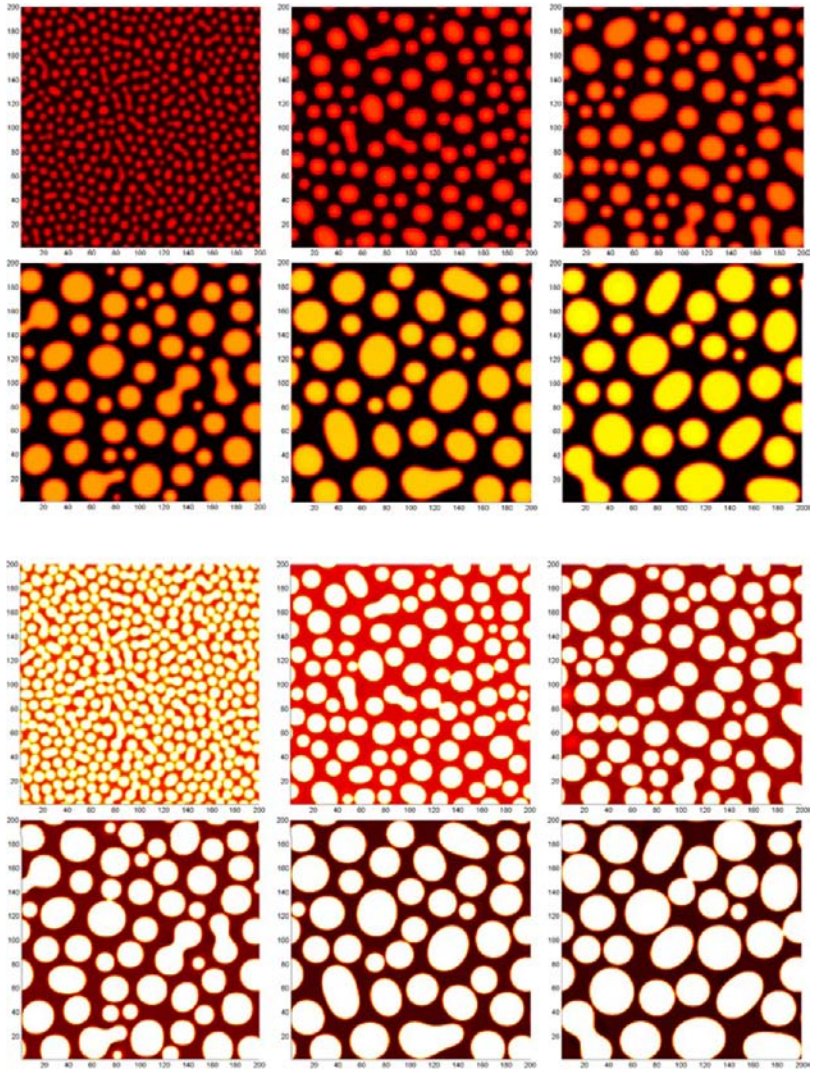

Figure 7. Simulated [70]PCBM volume fraction (φ_3) as a function of spatial coordinate for six sequential time intervals, calculated for $\chi_{13} = 0.1$. Image dimensions are arbitrary. In the top panel the color scale interpolates between $\varphi_3 = 0$ (black) and $\varphi_3 = 1$ (white); in the bottom panel between $\varphi_3 = 0$ (black) and $\varphi_3 = 0.1$ (white).

2.5. Simulating the Phase Separation in Time. Figure 7 shows the simulated temporal evolution of the phase separation for a blend of PDPP5T and [70]PCBM in chloroform solution. The starting composition was chosen just below the critical point with volume fractions at $t = 0$ of $\varphi_1 = 0.8$, $\varphi_2 = 0.086$, and $\varphi_3 = 0.114$, i.e., corresponding to a 1:2 (w/w) solids composition, assuming mass densities of 1 and 1.5 g/cm^3 for PDPP5T and [70]PCBM, respectively. This rather shallow quench depth corresponds to a relatively high solvent content to plausibly allow for sufficient mobility for demixing as well as subsequent coarsening to take place during film drying, as suggested by the experimental images (Figure 4).

The evaporation process was allowed to proceed after quenching by an algorithm that removed a quantity of solvent from the entire domain at each simulation time. Further details on the modeling algorithm are given in the Supporting Information. In the simulations we used $\chi_{13} = 0.4$, as calculated by eq 7 or $\chi_{13} = 0.1$, the value obtained when the entropic contribution χ_s in eq 7 is omitted. Both gave very similar behavior, and Figure 7 represents the data for $\chi_{13} = 0.1$. The images show dispersed [70]PCBM-enriched domains with globular shapes, characteristic to structure evolution in the liquid phase, dominated by capillary forces. The results qualitatively resemble the AFM and TEM images.

The reason for the dispersed nature of the [70]PCBM in a PDPP5T rich matrix, despite the total volumetric excess of [70]PCBM relative to PDPP5T, is the difference in solvent compatibility between the polymer and [70]PCBM. This is indicated by the tie lines in Figure 6, which tilt in favor of the polymer-rich phase. As a result, the polymer-rich phase will be more dilute than the [70]PCBM-rich phase. Mass conservation prescribes that the total volume of the polymer-rich phase should then be larger than the volume of the [70]PCBM-rich phase, explaining the dispersed nature of the latter. In the final stage of drying, which is not covered by the liquid-phase simulations, the polymer-rich phase collapses around the [70]PCBM domains, which is nicely demonstrated by the cross sectional TEM image (Figure 5). This partitioning phenomenon has also been reported to influence the morphology of liquid-phase demixed films of solvent-borne blends of polystyrene and poly(methyl methacrylate).[71]

To track the composition of the matrix phase as a function of time the [70]PCBM concentration is shown on a magnified color scale in the bottom panel of Figure 7). By interpolating

dx.doi.org/10.1021/ja405493j | J. Am. Chem. Soc. 2013, 135, 12057−12067

between φ_3 = 0 (black) and φ_3 = 0.1 (white), the dispersed [70]PCBM phase shows up white. In agreement with the phase diagram, the [70]PCBM concentration in the matrix phase *decreases* with time from φ_3 = 0.06 at early times to φ_3 = 0.015 at the end of the simulation, despite the blend becoming more concentrated due to solvent evaporation. The main reason for this is the fact that residual [70]PCBM in the matrix phase thermodynamically depletes as long as the system remains sufficiently mobile during film formation and solvent evaporation.

Close inspection of Figure 7 reveals that during coarsening of the phase separation the smaller, highly curved [70]PCBM domains temporarily redissolve into the matrix, to be subsequently absorbed by the larger domains. As a result, the domain number density decreases, but the average size increases. This process is a consequence of the fact that the residual [70]PCBM concentration in the vicinity of small domains is higher than in the vicinity of large domains.[72] As the average domain size increases according to $\langle R \rangle \sim t^{1/3}$, known as the Lifshitz−Slyozov law, it is expected that the contribution to the total [70]PCBM concentration in the matrix due to redissolution decreases with increasing residence time in the mobile state (i.e., drying time).

The simulations qualitatively reproduce the experimental morphologies and confirm that L−L demixing is the main cause for this type of morphology. The calculations also predict that the concentration of [70]PCBM decreases with drying time. As we will show in the next section, this prediction can be confirmed experimentally from the electrical characteristics of the blends for different thickness.

2.6. Charge Generation and Transport for Different Morphologies. Figure 8 shows the $J-V$ characteristics of the PDPP5T:[70]PCBM blends, spin coated from chloroform at different spin rates. The changes in the $J-V$ as a function of blend layer thickness are remarkable. Strikingly, the short-circuit current density *decreases* with increasing layer thickness, whereas usually one would expect it to increase as thicker layers absorb more light and thus generate more current. Figure 8 and Table 3 also show that the fill factor *increases* with increasing layer thickness. This is counterintuitive, because the fill factor usually decreases with increasing layer thickness due to an increased probability for bimolecular recombination when charges have to move over a longer distance before they can be collected. Figure 8 clearly shows that the thickest cells produce little current, but the charges that are created can be easily collected. The strong bias dependence of the current density observed for the thin layers is also remarkable. We verified that this is not due to leakage current.

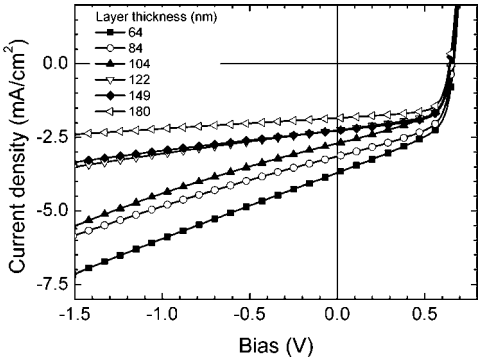

Figure 8. $J-V$ characteristics of the PDPP5T:[70]PCBM blend processed from chloroform as function of layer thickness.

Table 3. Solar Cell Parameters for PDPP5T:[70]PCBM Solar Cells Spin Coated from Chloroform at Different Layer Thickness

d (nm)	J_{sc} (mA/cm^2)	V_{oc} (V)	FF	PCE (%)
64	3.70	0.666	0.510	1.26
84	3.14	0.657	0.556	1.15
104	2.41	0.648	0.621	0.97
122	2.25	0.652	0.636	0.93
149	2.27	0.645	0.652	0.95
180	1.84	0.642	0.689	0.81

Closer inspection of Figure 8 suggests that the photocurrent consists of two components. One component that is rather independent of layer thickness, and one that seems to increase almost linearly with reverse bias in the range measured with a slope that is larger for thinner films. The explanation for this unusual behavior can be found in the composition of the blend that changes with layer thickness. The numerical simulations (Figures 7) suggest that for thin blends, with a shorter drying time, the films consist of many small [70]PCBM domains and a PDPP5T-rich matrix that contains a certain volume fraction of [70]PCBM. For thicker films, that need more time to dry, the [70]PCBM domains grow in size and the concentration of [70]PCBM in the matrix decreases. The AFM and TEM images (Figure 4) confirm the changing size of the domains but give no information about the [70]PCBM concentration in the blend. We propose that the change in [70]PCBM concentration is reflected in the shape $J-V$ curve. In the thick blends excitons created by absorption of a photon will predominantly dissociate into charge carriers at the interface between the two relatively pure phases. These charges are easy to collect, owing to the high purity of the phases through which they drift and diffuse and in which they are unlikely to recombine because oppositely charged carriers are absent. This is the origin of the high fill factor for thick films. On the other hand, for thin blend layers charges will also be generated in the PDPP5T-rich matrix because it contains an appreciable amount of finely dispersed or possibly molecularly mixed [70]PCBM. The negative charges created on the [70]PCBM molecules in the matrix are more difficult to collect, when the concentration of [70]PCBM is low and does not provide efficient percolating pathways. These charges will experience a strong electric field-dependent mobility, resulting in a photocurrent that increases with reverse bias. A similar dual charge generation−collection mechanism was recently proposed to explain the current−voltage characteristics of polymer:fullerene (MDMO-PPV:[60PCBM) bulk heterojunction solar cells at different degrees of nanoscale phase separation.[73] A schematic drawing for the different charge generation and collection mechanisms in thin and thick films is shown in Figure 9.

To find additional experimental evidence for the proposed dual charge generation and collection mechanisms processes, we performed external quantum efficiency (EQE) measurements as function of applied external bias (V) for three cells with increasing layer thickness (85, 159, and 246 nm) (Figure 10). These EQE−V experiments reveal that for thinner layers the contribution of the PDPP5T absorption in 600−850 nm wavelength range to the photocurrent increases significantly relative to that of the contribution of [70]PCBM in the 400−600 nm range at higher reverse electrical bias. This indicates

dx.doi.org/10.1021/ja405493j | J. Am. Chem. Soc. 2013, 135, 12057−12067

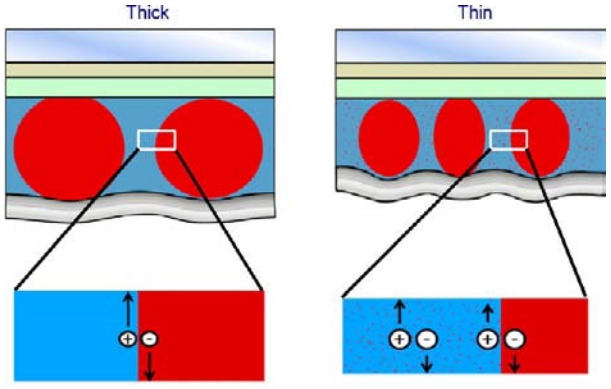

Figure 9. Charge generation and collection in thick and thin blend layers of PDPP5T (blue) and [70]PCBM (red) blend layers cells. For the thick layers, charges are predominantly created at the interface between the large domains, and for thin layers, additional charges are created in the PDPP5T domains that contain a larger amount of [70]PCBM. These latter charges are more difficult to extract.

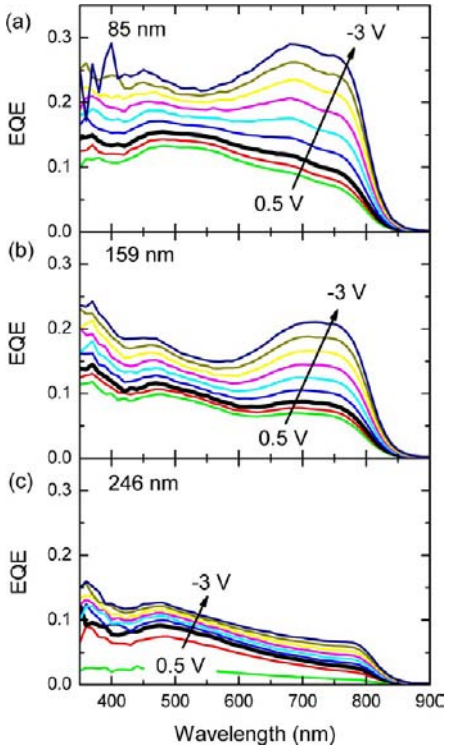

Figure 10. EQE vs wavelength for different bias voltages of PDPP5T:[70]PCBM blends spin coated from chloroform at different layer thickness: (a) 85, (b) 159, (c) 246 nm. The thick black line represents 0 V bias.

that the bias-dependent charges in the $J-V$ characteristics predominantly originate from the higher wavelengths, i.e., corresponding to the polymer-rich phase. This observation supports the proposal that residual amount of [70]PCBM in the polymer-rich phase causes the bias-dependent current.

The remaining question is: how much [70]PCBM is dispersed in the polymer causing this effect? To experimentally estimate the amount of residual [70]PCBM, we mimicked the matrix phase by adding an increasing amount of [70]PCBM to the mixture from 0 to 45 wt %, while the optimized blends have 66 wt %. The PDPP5T concentration in the spin coating solution and the final layer thickness were kept constant. Figure 11 shows that for low weight percentages of PCBM, the slope of the $J-V$ at bias $V < 0.5$ V is increasing with increasing weight

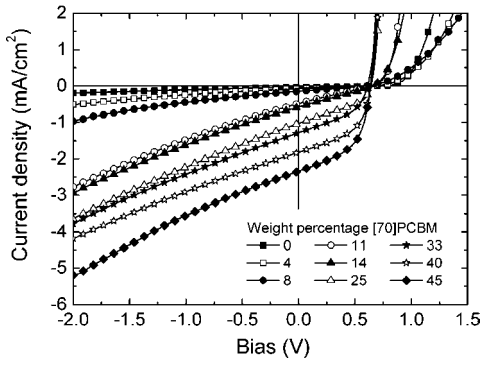

Figure 11. $J-V$ curves of PDPP5T:[70]PCBM cells spin coated from chloroform with low [70]PCBM weight fractions.

percentage. For weight percentages >11%, the slope saturates. From that point on larger agglomerates of [70]PCBM are formed, as was confirmed by an increased corrugation of the surface of the film observed with AFM (not shown). The total current still increases as well as the fill factor. Starting from 25% the series resistance (inverse slope at $J = 0$) does not increase anymore, indicating that the morphology is similar to the optimal one. As indicated by the red arrows in the phase diagram (Figure 6), 11% of [70]PCBM (1:0.12 (w/w) blend ratio) and 25% of [70]PCBM (1:0.33 (w/w) blend ratio) correspond to quenches near or in the metastable region of the phase diagram, suggesting that for those blend ratio's the observed [70]PCBM agglomerates may form via nucleation-and-growth rather than spinodal decomposition.

3. CONCLUSION

Film formation in OPV blends of PDPP5T and [70]PCBM spin-cast from chloroform has been studied experimentally using AFM and TEM microscopy. The temporal evolution of the phase separation was effectively described by a model that uses the homogeneous Flory–Huggins free energy of the of the solvent:polymer:fullerene mixture and accounts for interfacial interactions between separated phases, based on physical properties of the components. From the experiment and model we conclude that for blends of PDPP5T and [70]PCBM, spin coated from chloroform, the phase separation in the thin film results from L–L demixing during the drying of the film. The large, rather pure, [70]PCBM domains formed in these blends, that protrude from the film surface when dry, result from a liquid droplet phase that (mainly) contains solvent and [70]PCBM. This liquid droplet phase has separated via spinodal demixing from the second continuous phase that contains solvent, PDPP5T, and [70]PCBM. For longer drying times, i.e., for thicker films, the large droplets grow at the expense of smaller droplets via Ostwald ripening, and the amount of [70]PCBM in the continuous phase decreases. The model consistently explains the microscopy (AFM and TEM) of these blends and the $J-V$ and EQE$-V$ measurements on the corresponding solar cells.

Because the large [70]PCBM domains observed in PDPP5T:[70]PCBM films spin coated from chloroform are characteristic for the phase separation in numerous other polymer:fullerene blends cast from single solvent,[11−13,26−37] we think that the spinodal L–L demixing and the time evolution are universal for

dx.doi.org/10.1021/ja405493j | J. Am. Chem. Soc. 2013, 135, 12057−12067

many of the polymers developed for OPV applications. We note, however, that exceptions exist, e.g., P3HT,[21] PCPDTBT,[14] and PSBTBT[20] do generally not lead to L−L demixing when mixed with [60] or [70]PCBM. Moreover, our model does not describe how the addition of a processing additive or co-solvent, sometimes in small amounts, can change the morphology completely (cf. Figure 3).

In the future, the model could be expanded to four components to include the co-solvent. Ideally, this model can be then be used as a predictive one: by measuring certain properties of a newly synthesized polymer one can know beforehand which conditions to use in solar cell fabrication, to gain an optimal morphology and optimized performance.

■ ASSOCIATED CONTENT

Supporting Information

Experimental details on materials, methods, and simulations are provided. This material is available free of charge via the Internet at http://pubs.acs.org.

■ AUTHOR INFORMATION

Corresponding Author

r.a.j.janssen@tue.nl

Notes

The authors declare no competing financial interest.

■ ACKNOWLEDGMENTS

We thank Niek Lousberg and Kirill Arapov for making the cross-section samples for TEM imaging and Alice Furlan and Hans van Franeker for TEM measurements. This work forms part of the Joint Solar Programme (JSP) and of the Stichting voor Fundamenteel Onderzoek der Materie (FOM), which is supported financially by Nederlandse Organisatie voor Wetenschappelijk Onderzoek (NWO). This work is co-financed by Hyet Solar. The research leading to these results has received funding from the Ministry of Education, Culture and Science (Gravity program 024.001.035) and is further part of the research program of the Dutch Polymer Institute (DPI project 660) and the Solliance Organic Photovoltaics Programme.

■ REFERENCES

(1) He, Z. C.; Zhong, C. M.; Su, S. J.; Xu, M.; Wu, H. B.; Cao, Y. *Nat. Photonics.* **2012**, *6*, 591−595.

(2) You, J.; Dou, L.; Yoshimura, K.; Kato, T.; Ohya, K.; Moriarty, T.; Emery, K.; Chen, C.-C.; Gao, J.; Li, G.; Yang, Y. *Nat. Commun.* **2013**, *4*, 1446.

(3) Sondergaard, R.; Hosel, M.; Angmo, D.; Larsen-Olsen, T. T.; Krebs, F. C. *Mater. Today* **2012**, *15*, 36−49.

(4) Cheng, Y. J.; Yang, S. H.; Hsu, C. S. *Chem. Rev.* **2009**, *109*, 5868−5923.

(5) Duan, C.; Huang, F.; Cao, Y. *J. Mater. Chem.* **2012**, *22*, 10416−10434.

(6) Facchetti, A. *Chem. Mater.* **2011**, *23*, 733−758.

(7) Bavel, S.; Veenstra, S.; Loos, J. *Macromol. Rapid Commun.* **2010**, *31*, 1835−1845.

(8) Brabec, C. J.; Heeney, M.; McCulloch, I.; Nelson, J. *Chem. Soc. Rev.* **2011**, *40*, 1185−1199.

(9) Liu, F.; Gu, Y.; Jung, J. W.; Jo, W. H.; Russell, T. P. *J. Polym. Sci., Part B* **2012**, *50*, 1018−1044.

(10) Ruderer, M. A.; Mueller-Buschbaum, P. *Soft Matter* **2011**, *7*, 5482−5493.

(11) Shaheen, S. E.; Brabec, C. J.; Sariciftci, N. S.; Padinger, F.; Fromherz, T.; Hummelen, J. C. *Appl. Phys. Lett.* **2001**, *78*, 841−843.

(12) Zhang, F.; Jespersen, K. G.; Bjoerström, C.; Svensson, M.; Andersson, M. R.; Sundström, V.; Magnusson, K.; Moons, E.; Yartsev, A.; Inganäs, O. *Adv. Funct. Mater.* **2006**, *16*, 667−674.

(13) Wienk, M. M.; Turbiez, M.; Gilot, J.; Janssen, R. A. J. *Adv. Mater.* **2008**, *20*, 2556−2560.

(14) Peet, J.; Kim, J. Y.; Coates, N. E.; Ma, W. L.; Moses, D.; Heeger, A. J.; Bazan, G. C. *Nat. Mater.* **2007**, *6*, 497−500.

(15) Li, G.; Shrotriya, V.; Huang, J.; Yao, Y.; Moriarty, T.; Emery, K.; Yang, Y. *Nat. Mater.* **2005**, *4*, 864−868.

(16) Schmidt-Hansberg, B.; Sanyal, M.; Klein, M. F. G.; Pfaff, M.; Schnabel, N.; Jaiser, S.; Vorobiev, A.; Müller, E.; Colsmann, A.; Scharfer, P.; Gerthsen, D.; Lemmer, U.; Barrena, E.; Schabel, W. *ACS Nano* **2011**, *5*, 8579−8590.

(17) Padinger, F.; Rittberger, R. S.; Sariciftci, N. S. *Adv. Funct. Mater.* **2003**, *13*, 85−88.

(18) Campoy-Quiles, M.; Ferenczi, T.; Agostinelli, T.; Etchegoin, P. G.; Kim, Y.; Anthopoulos, T. D.; Stavrinou, P. N.; Bradley, D. D. C.; Nelson, J. *Nat. Mater.* **2008**, *7*, 158−164.

(19) DeLongchamp, D. M.; Kline, R. J.; Herzing, A. *Energy Environ. Sci.* **2012**, *5*, 5980−5993.

(20) Schmidt−Hansberg, B.; Klein, M. F. G.; Sanyal, M.; Buss, F.; de Medeiros, G. Q. G.; Munuera, C.; Vorobiev, A.; Colsmann, A.; Scharfer, P.; Lemmer, U.; Barrena, E.; Schabel, W. *Macromolecules* **2012**, *45*, 7948−7955.

(21) Yang, X.; Veenstra, S. C.; Verhees, W. J. H.; Wienk, M. M.; Janssen, R. A. J.; Kroon, J. M.; Michels, M. A. J.; Loos, J. *Nano Lett.* **2005**, *5*, 579−583.

(22) Moulé, A. J.; Meerholz, K. *Adv. Mater.* **2008**, *20*, 240−245.

(23) Peet, J.; Cho, N. S.; Lee, S. K.; Bazan, G. C. *Macromolecules* **2008**, *41*, 8655−8659.

(24) Lee, J. K.; Ma, W. L.; Brabec, C. J.; Yuen, J.; Moon, J. S.; Kim, J. Y.; Lee, K.; Bazan, G. C.; Heeger, A. J. *J. Am. Chem. Soc.* **2008**, *130*, 3619−3623.

(25) Coates, N. E.; Hwang, I. W.; Peet, J.; Bazan, G. C.; Moses, D.; Heeger, A. J. *Appl. Phys. Lett.* **2008**, *93*, 0721051/1−3.

(26) Martens, T.; D'Haen, J.; Munters, T.; Beelen, Z.; Goris, L.; Manca, J.; D'Olieslaeger, M.; Vanderzande, D.; De Schepper, L.; Andriessen, R. *Synth. Met.* **2003**, *138*, 243−247.

(27) Van Duren, J. K. J.; Yang, X.; Loos, J.; Bulle-Lieuwma, C. W. T.; Sieval, A. B.; Hummelen, J. C.; Janssen, R. A. J. *Adv. Funct. Mater.* **2004**, *14*, 425−434.

(28) Hoppe, H.; Niggemann, M.; Winder, C.; Kraut, J.; Hiesgen, R.; Hinsch, A.; Meissner, D.; Sariciftci, N. S. *Adv. Funct. Mater.* **2004**, *14*, 1005−1011.

(29) Wienk, M. M.; Kroon, J. M.; Verhees, W. J. H.; Knol, J.; Hummelen, J. C.; van Hal, P. A.; Janssen, R. A. *J Angew. Chem. Int. Ed.* **2003**, *42*, 3371−3375.

(30) Nilsson, S.; Bernasik, A.; Budkowski, A.; Moons, E. *Macromolecules* **2007**, *40*, 8291−8301.

(31) Andersson, B. V.; Herland, A.; Masich, S.; Inganäs, O. *Nano Lett.* **2009**, *9*, 853−855.

(32) Bijleveld, J. C.; Gevaerts, V. S.; Di Nuzzo, D.; Turbiez, M.; Mathijssen, S. G. J.; de Leeuw, D. M.; Wienk, M. M.; Janssen, R. A. J. *Adv. Mater.* **2010**, *22*, E242−E246.

(33) Amb, C. M.; Chen, S.; Graham, K. R.; Subbiah, J.; Small, C. E.; So, F.; Reynolds, J. R. *J. Am. Chem. Soc.* **2011**, *133*, 10062−10065.

(34) Collins, B. A.; Li, Z.; Tumbleston, J. R.; Gann, E.; McNeill, C. R.; Ade, H. *Adv. Energy Mater.* **2013**, *3*, 65−74.

(35) Wang, E. G.; Ma, Z.; Zhang, Z.; Vandewal, K.; Henriksson, P.; Inganäs, O.; Zhang, F.; Andersson, M. R. *J. Am. Chem. Soc.* **2011**, *133*, 14244−12447.

(36) Wang, E. G.; Ma, Z.; Zhang, Z.; Henriksson, P.; Inganäs, O.; Zhang, F.; Andersson, M. R. *Chem. Commun.* **2011**, *47*, 4908−4910.

(37) Stalder, R.; Grand, C.; Subbiah, J.; So, F.; Reynolds, J. R. *Polym. Chem.* **2012**, *3*, 89−92.

(38) Small, C. E.; Chen, S.; Subbiah, J.; Amb, C. M.; Tsang, S.-W.; Lai, T.-H.; Reynolds, J. R.; So, F. *Nat. Photonics* **2012**, *6*, 115−120.

(39) Hendriks, K. H.; Heintges, G. H. L.; Gevaerts, V. S.; Wienk, M. M.; Janssen, R. A. J. *Angew. Chem., Int. Ed.* **2013**, DOI: 10.1002/anie.201302319.
(40) Cabanetos, C.; El Labban, A.; Bartelt, J. A.; Douglas, J. D.; Mateker, W. R.; Fréchet, J., M. J.; McGehee, M. D.; Beaujuge, P. M. *J. Am. Chem. Soc.* **2013**, *135*, 4656−4659.
(41) Gevaerts, V. S.; Furlan, A.; Wienk, M. M.; Turbiez, M.; Janssen, R. A. J. *Adv. Mater.* **2012**, *24*, 2130−2134.
(42) Kouijzer, S.; Esiner, S.; Frijters, C. H.; Turbiez, M.; Wienk, M. M.; Janssen, R. A. J. *Adv. Energy Mater.* **2012**, *2*, 945−949.
(43) Li, W. W.; Hendriks, K. H.; Roelofs, W. S. C.; Kim, Y.; Wienk, M. M.; Janssen, R. A. J. *Adv. Mater.* **2013**, *25*, 3182−3186.
(44) Cahn, J. W.; Hilliard, J. E. *J. Chem. Phys.* **1958**, *28*, 258−266.
(45) Cahn, J. W. *Acta Metall.* **1961**, *9*, 795−805.
(46) Huang, C.; Olvera de la Cruz, M.; Swift, B. W. *Macromolecules* **1995**, *28*, 7996−8005.
(47) Saylor, D. M.; Kim, C.−S.; Patwardhan, D. V.; Warren, J. A. *Acta Biomater.* **2007**, *3*, 851−864.
(48) Flory, P. J. *Principles of Polymer Chemistry*; Cornell University Press: Ithaca, NY, 1953.
(49) Cook, H. E. *J. Phys. Chem. Solids* **1969**, *30*, 2427−2437.
(50) Cook, H. E. *Acta Metall.* **1970**, *18*, 297−306.
(51) Jones, R. A. L.; Richards, R. W. *Polymers at Surfaces and Interfaces*; Cambridge University Press: Cambridge, UK, 1999, p 158.
(52) Krausch, G.; Dai, C. A.; Kramer, E. J.; Marko, J. F.; Bates, F. S. *Macromolecules* **1993**, *26*, 5566−5571.
(53) Jones, R. A. L. *Phys. Rev. E* **1993**, *47*, 1437−1440.
(54) Geoghegan, M.; Jones, R. A. L.; Clough, A. S. *J. Chem. Phys.* **1995**, *103*, 2719−2724.
(55) Henderson, I. C.; Clarke, N. *Macromol. Theory Simul.* **2005**, *14*, 435−443.
(56) Yan, L−. T.; Xie, X. M. *Macromolecules* **2006**, *39*, 2388−2397.
(57) Michels, J. J. *ChemPhysChem* **2011**, *12*, 342−348.
(58) Björström, C. M.; Bernasik, A.; Rysz, J.; Budkowski, A.; Nilsson, S.; Svensson, M.; Andersson, M. R.; Magnusson, K. O.; Moons, E. *J. Phys.: Condens. Matter* **2005**, *17*, L529−L534.
(59) Björström, C. M.; Nilsson, S.; Bernasik, A.; Budkowski, A.; Andersson, M.; Magnusson, K. O.; Moons, E. *Appl. Surf. Sci.* **2007**, *253*, 3906−3912.
(60) Anselmo, A. S.; Lindgren, L.; Rysz, J.; Bernasik, A.; Budkowski, A.; Andersson, M. R.; Svensson, K.; van Stam, J.; Moons, E. *Chem. Mater.* **2011**, *23*, 2295−2302.
(61) See: Żenkiewicz, M. *J. Achiev. Mater. Manuf. Eng.* **2007**, *24*, 137−145 and references cited therein..
(62) *Polymer Handbook*; Brandrup, J.; Immergut, E. H.; Grulke. E. A., Eds.: Wiley: New York, 1999.
(63) Germack, D. S.; Chan, C. K.; Hamadani, B. H.; Richter, L. J.; Fischer, D. A.; Gundlach, D. J.; DeLongchamp, D. M. *Appl. Phys. Lett.* **2009**, *94*, 233303.
(64) Machui, F.; Langner, S.; Zhu, X.; Abbott, S.; Brabec, C. J. *Sol. Energy Mater. Sol. Cells* **2012**, *100*, 138−146.
(65) Grell, M.; Bradley, D. D. C.; Long, X.; Chamberlain, T.; Inbasekaran, M.; Woo, E. P.; Soliman, M. *Acta Polym.* **1998**, *49*, 439−444.
(66) Kim, J. S.; Lee, Y. M.; Lee, J. H.; Park, J. H.; Kim, J. K.; Cho, K. *Adv. Mater.* **2010**, *22*, 1355−1360.
(67) Chung, D. S.; Kong, H.; Yun, W. M.; Cha, H.; Shim, H.−K.; Kim, Y.−H.; Park, C. E. *Org. Electron.* **2010**, *11*, 899−904.
(68) Barton, A. F. M. *CRC Handbook of Solubility Parameters and Other Cohesion Parameters*, CRC Press: Boca Raton, Fla. 1985.
(69) ACD LABS Freeware (see: http://www.acdlabs.com/resources/freeware/chemsketch/).
(70) Taking the number, versus the weight, average molecular weight as the basis for these calculations did not result in sufficiently different values for N_2 to significantly influence the free energy curve or the phase diagram.
(71) Walheim, S.; Boltau, M.; Mlynek, J.; Krausch, G.; Steiner, U. *Macromolecules* **1997**, *30*, 4995−5003.
(72) Jones, R. A. L. *Soft Condensed Matter*; Oxford University Press: Oxford, UK, 2002.
(73) Maturová, K.; van Bavel, S. S.; Wienk, M. M.; Janssen, R. A. J.; Kemerink, M. *Nano Lett.* **2009**, *9*, 3032−3037.